Engineering Nano-Composite Interlayer for Novel Ceramic-based Forward Osmosis Membrane with Enhanced Performance

Mingming Zhang[a], Wenbiao Jin[d], Fenglin Yang[a], Mikel Duke[c], Yingchao Dong[a]*, Chuyang Y. Tang[b]**

[a] Key Laboratory of Industrial Ecology and Environmental Engineering (Ministry of Education, MOE), School of Environmental Science and Technology, Dalian University of Technology, Dalian 116024, China

[b] Department of Civil Engineering, The University of Hong Kong, Pokfulam, Hong Kong, China

c Institute for Sustainable Industries & Liveable Cities, Victoria University, PO Box 14428, Melbourne, Australia

d School of Civil and Environmental Engineering, Harbin Institute of Technology, Shenzhen 518055, China

***Corresponding author**:

Prof. Chuyang Y. Tang
Department of Civil Engineering, The University of Hong Kong, Pokfulam, Hong Kong, China
Tel: +86-852-28591976 E-mail: tangc@hku.hk.

Prof. Yingchao Dong
Key Laboratory of Industrial Ecology and Environmental Engineering (Ministry of Education, MOE), School of Environmental Science and Technology, Dalian University of Technology, Dalian 116024, China
Tel: +86-411-84706328 E-mail: ycdong@dlut.edu.cn

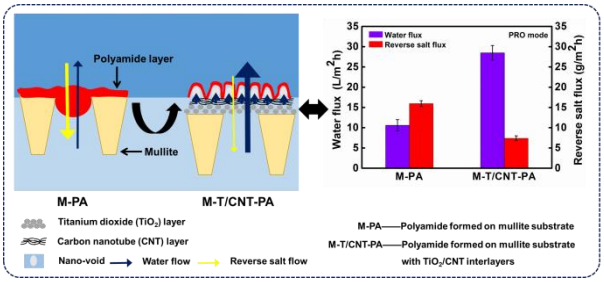

Graphical abstract

ABSTRACT

Rational design of high-performance defect-free polyamide (PA) layer on robust ceramic substrate is challenging for forward osmosis (FO) water treatment applications. In this study, we first demonstrated a robust ceramic-based thin-film composite (TFC) FO membrane by engineering a novel nano-composite interlayer of titanium dioxide and carbon-nanotube (TiO_2/CNT). The structural morphologies and properties were systematically characterized for different substrates (without interlayer, with TiO_2 interlayer, or with TiO_2/CNT interlayer) and the corresponding ceramic-based TFC-FO membranes. Introduction of low roughness nano-composite interlayers with decreased pore size created an interface with improved surface characteristics, favoring the formation of a defect-free nano-voids-containing PA layer with high cross-linking degree. The resulting ceramic-based FO membrane had a water permeability of approximately 2 L/(m^2 h bar) and a NaCl rejection of 98%, showing simultaneous enhancements in both compared to the control membrane without interlayer. Mechanism analysis indicates that such a special nano-composite interlayer not only provided more active cites for the formation of thinner defect-free nano-voids-containing PA layer without penetration into substrate, but acted as a highly porous three dimension network structure for rapid water transport. This work provides a novel protocol for rational design and fabrication of high performance multi-layered inorganic FO membrane as well as extended applications in water treatment with enhanced performance.

INTRODUTION

Desalination is a reliable option to obtain freshwater from unconventional sources such as seawater, brackish groundwater, and wastewater for mitigating the challenge of water scarcity that is expected to affect approximately 4 billion people globally in the coming decades.[1] Compared with other desalination technologies such as reverse osmosis (RO)[2] and membrane distillation,[3] osmotically-driven forward osmosis (FO) offers potential advantages of greater tolerance to membrane fouling, higher available water recovery and low energy consumption, in addition to its nearly complete rejection to a wide range of contaminants.[4-6] These features make FO particularly interesting for challenging applications with high fouling/scaling propensity, such as zero liquid discharge,[7] produced water treatment,[6] FO-membrane bioreactor[8] etc. However, development of FO desalination technology requires high performance FO membranes.

Literature on FO membrane development in the last decade has largely focused on strategies of mitigating internal concentration polarization (ICP), i.e., the concentration polarization inside membrane substrate that causes a substantial loss of effective osmotic driving force.[9-12] Meanwhile, the development of thin-film composite (TFC) polyamide (PA) FO membranes has resulted in significant enhancement in membrane water permeability and selectivity.[13] For example, polyamide FO membranes have been prepared on various polymeric substrates, such as cellulose acetate,[14] polysulfone,[15] polyethersulfone,[16] and polybenzimidazole.[17] Nevertheless, these polymeric substrates often suffer from their low mechanical

strength, insufficient thermal and chemical stability, and/or poor hydrophilicity,[18] which prevents their uses for challenging applications for which FO would otherwise offer competitive advantages. The limitation of existing FO membranes prompts us to design more robust membranes.

Presumably, inorganic ceramic substrates have a great potential for the preparation of high-performance FO membranes, thanks to their excellent mechanical, chemical and thermal stability, hydrophilicity and anti-fouling properties.[19-22] To date, however, ceramic-based FO membranes have not yet been reported in the literature. The relatively low porosity of conventional ceramic substrates[23] will likely cause serious ICP for FO applications. The relatively coarse surfaces of ceramic substrates present another critical challenge to the formation of high-quality PA rejection layer with high water permeability and salt rejection, since the interfacial polymerization reaction used for PA synthesis is highly sensitive to the surface characteristics of the substrates.[24-28]

In this study, we report a novel high performance PA-ceramic FO membrane featuring a nano-composite interlayer. A dry-wet spinning technique followed by sintering was used to create a highly porous mullite substrate structure (Figure 1). A nano-composite TiO_2/CNT interlayer was prepared on this ceramic substrate to optimize its surface morphology, pore size and roughness for improved subsequent growth of the PA rejection layer. We demonstrate that an enhanced roughness structure of the resulting PA layer, combined with a highly porous structural feature of the interlayer, resulted in higher water flux and lower reverse salt flux, outperforming

the control membrane without interlayer as well as other state-of-the-art FO membranes. A membrane formation and transportation mechanism was proposed to understand on how high-quality PA layer can be constructed on coarse ceramic substrate to finally form ceramic-based FO membranes featuring excellent application performance such as water permeability and salt rejection.

MATERIALS AND METHODS

Fabrication of Mullite Substrate. The mullite hollow fiber substrate (labeled as M) was prepared through a dry-wet-spinning technique with the immersion-induced phase inversion process (Figure 1) based on optimized dope compositions and spinning conditions (Supporting Information Section S1, Figures S1 and S2, Tables S1 and S2).

Fabrication of Nano-composite TiO_2/CNT Interlayers. The preparation processes of TiO_2 and CNT suspension are given in Figure 1 and Supporting Information S1.3. The mullite substrate was dipped into the suspension for 5 s and taken out immediately and carefully, followed by complete drying at ambient temperature. Subsequently, the mullite substrate coated with TiO_2 was sintered at 800 °C for 2 h (heating rate of 1 °C/min), which was labeled as M-T. In our work, rutile-phase TiO_2 was formed as an interlayer when sintered at 800 °C for 2 h. Such a sintering temperature was required to assure good adhesion between the TiO_2 layer and the mullite substrate as well as the long-term mechanical stability of the TiO_2 layer.[21] The key function of this TiO_2 interlayer was to modify surface pore size and roughness, providing a substrate featuring better surface characteristics (i.e., smoother

surface with smaller pores) for the formation of a high-quality CNT layer. The CNT interlayer was fabricated by vacuum filtration method, whose thicknesses were determined by controlling filtration time (10 s, 20 s, 40 s, 60 s). To enhance the stability of the CNT layer, surface modification by polydopamine was applied (Supporting Information S1.3.2). The prepared MWCNTs suspension was vacuum-filtered onto the M-T substrate to form a CNT layer by applying a vacuum of 0.8 bar at the lumen side of the hollow fibers. Finally, to increase the binding between substrate and CNTs, the mullite substrates coated with TiO_2/CNT interlayers were cured in an oven at 60 °C for 10 min.[29] During drying-curing process, highly adhesive cross-linked polydopamine was formed via polymerization reaction of dopamine at weakly basic conditions, efficiently enhancing both CNT/TiO_2 interfacial bonding and cross-linking between CNTs.[30,31] The mullite substrate coated with TiO_2/CNT interlayers was labeled as M-T/CNT.

Fabrication of Ceramic-based TFC-FO Membranes. The polyamide (PA) selective layer was fabricated on the outer surface of the ceramic-based substrates (M, M-T and M-T/CNT) via interfacial polymerization (IP, Figure 1). Detailed optimization of monomer compositions is shown in Figures S7 and S8, where a 5 wt% MPD and 0.4 wt/v% TMC/n-hexane solution were used in all subsequent experiments. The final TFC-FO membranes are denoted as M-PA, M-T-PA and M-T/CNT-PA, respectively. More details about the formation of polyamide selective layer are given in the Supporting Information S1.4.

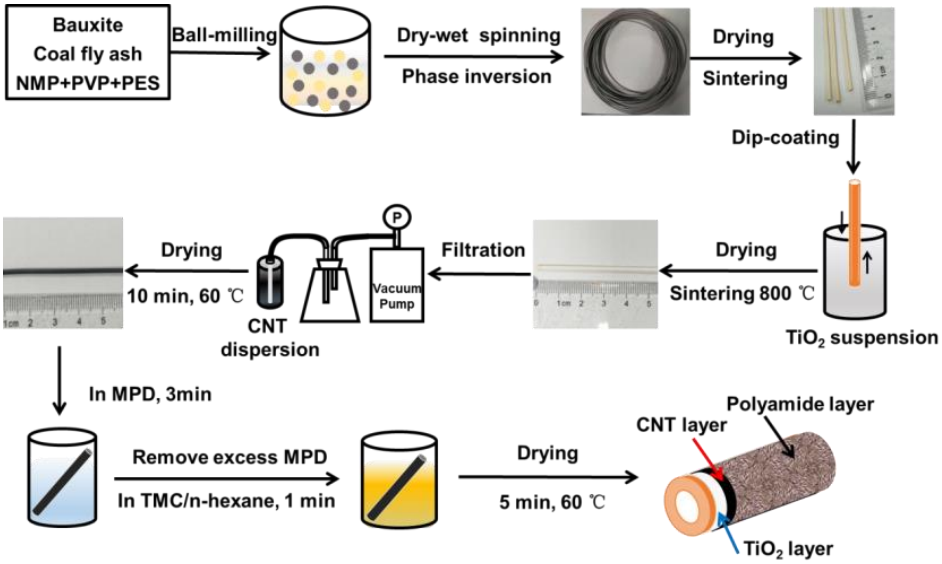

166

167 **Figure 1.** Schematic diagram of the preparation process of ceramic-based FO membrane with

168 TiO_2/CNT nano-composite interlayers.

169 **Membrane Characterization.** The surface and cross-sectional morphologies of

170 the prepared substrates and TFC-FO membranes were observed using scanning

171 electron microscopy (SEM, QUANTA 450, FEI, America) and field emission

172 scanning electron microscope (FESEM, S-4800, Hitachi, Japan) equipped with energy

173 dispersive spectrometer (EDS) mapping analysis. X-ray photoelectron spectroscopy

174 (XPS, K-Alpha+) was used to determine the elemental composition and cross-linking

175 degree of the PA selective layers. To characterize the surface hydrophilicity of the

176 substrates and TFC-FO membranes, water contact angle (WCA) measurements were

177 performed using a dynamic contact angle goniometer (PT-705, Guangdong

178 Zhongcheng Pussett Equipment Co., Ltd., China). Atomic force microscopy (AFM,

179 Dimension Icon, Bruker, America) was used to measure the membrane surface

180 roughness. The mean pore size and pore size distribution of the substrates with and

181 without interlayer were measured by a porometer (PSDA-20, Nanjing GaoQ

Functional Material Co., Ltd., China). The surface porosity of the substrates was quantified from their SEM images using ImageJ software (National Institutes of Health, America). The mechanical properties of the membrane substrates were measured by electronic universal testing machine (AGS-X, Shimadzu (Suzhou) Instruments Manufacturing Co., Ltd., China).

Membrane Performance Evaluation. A dead-end permeation cell in the RO mode was employed to measure the water permeability coefficient (A), salt permeability coefficient (B) and salt rejection (R_s) of the ceramic-based TFC-FO membranes. The FO performance of ceramic-based TFC-FO membranes (M-PA, M-T-PA and M-T/CNT-PA) was conducted with a lab-scale FO setup (Figure S3). DI water was used as feed solution (FS) while NaCl aqueous solutions with various concentrations (0.5–2.0 M) were used as draw solutions (DS). The membrane performance test was conducted in two different operational modes: FO mode (where PA layer faced to FS) and pressure retarded osmosis mode (PRO, where draw solution flowed against PA layer). More details about the performance evaluation of ceramic-based TFC-FO membranes can be found in the Supporting Information S1.5.

RESULTS AND DISCUSSION

Design of Nano-composite Interlayer

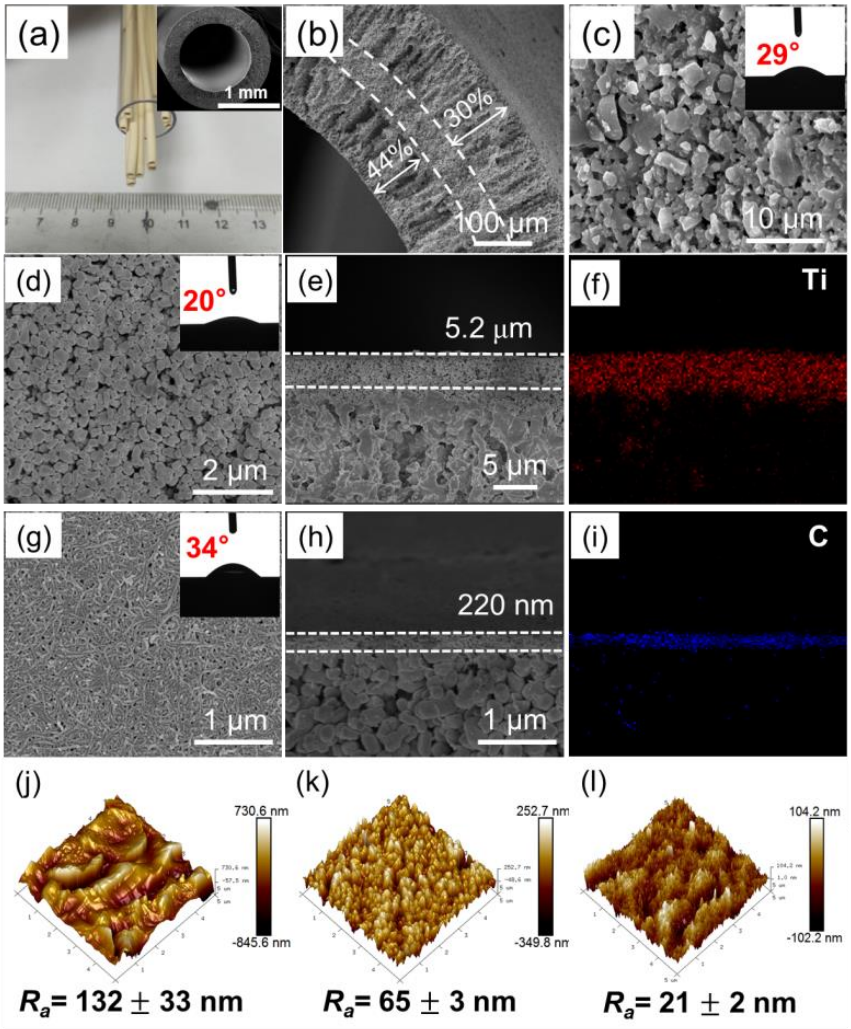

Figure 2. (a) Photograph (with cross-sectional SEM image inserted), (b) locally enlarged cross-sectional SEM and (c) outer surface SEM images of mullite membrane substrates (M); (d) surface SEM, (e) cross sectional SEM and (f) EDS mapping image (red, Ti element) of the mullite substrate with TiO_2 interlayer (M-T); (g) surface SEM, (h) cross sectional SEM and (i) EDS mapping image (blue, C element) of the mullite substrate with nano-composite TiO_2/CNT interlayers (M-T/CNT); and surface AFM images of various substrates: (j) M, (k) M-T and (l) M-T/CNT. The insets of (c), (d) and (g) present the contact angle results of M, M-T, and M-T/CNT, respectively.

The dry-wet spinning technique was used to prepare a mullite substrate of a highly asymmetric structure (Figure 2),[32] whose structure morphology, surface porosity and mechanical properties can be finetuned using different sintering temperatures (Figures S4 and S5). Compared to commercial alumina ceramic membranes, the mullite substrates are more cost competitive due to the use of less expensive ceramic powers and lower sintering temperature (Supporting Information S3). After sintering, hollow fiber mullite substrates have pale-yellow color (Figure 2a) due to the presence of Fe_2O_3 (3.81 wt%) in the starting material (Table S1). The substrates exhibited a finger-sponge-finger asymmetric structure consisting of long inner and outer finger-like macro-voids (74% of the overall thickness of 260 ± 2 μm) and an intermediate sponge-like layer (26%) sandwiched in between (Figure 2b). Hydrodynamically unstable viscous fingering phenomenon played a key role on the formation of such an asymmetric structure in hollow fiber ceramic membranes (Supporting Information S4).[33] Uniform porous structure was formed for outer surface with a surface porosity of 22 ± 1.2% (Figure 2c). These structural features (thin thickness, straight finger-like macro-voids and high surface porosity) are beneficial to reduce ICP by lowering the structure parameter. At the same time, the sandwiched sponge-like layer provides excellent mechanical stability of the substrate.[21] However, due to their large surface pores (mean pore size ~ 475 ± 24 nm, Figure S6a) and high roughness (R_a ~ 132 ± 33 nm, Figure 2j), it was difficult to form a thin PA layer on the coarse mullite ceramic substrate. To address this issue, TiO_2 (~ 5.2 μm thickness, Figures 2d-f) and CNT (~ 0.22 μm thickness, Figures 2g-i) interlayers were

successively coated on coarse mullite substrate to tune its surface properties, with the TiO_2 interlayer used to prevent the penetration of CNT into mullite substrate. Compared ullite substrate, such a nano-composite TiO_2/CNT interlayer exhibits a smoother surface (R_a ~ 65 ± 3 nm for M-T and 21 ± 2 nm for M-T/CNT, Figures 2k-l) with smaller pore size (~ 375 ± 14 nm for M-T and 150 ± 10 nm for M-T/CNT, Figure S6a), respectively. Moreover, coating of TiO_2/CNT interlayers on the coarse mullite substrate had no major adverse impact on its surface porosity, mechanical and hydrophilic properties (Figures S6b-d). Consequently, introduction of TiO_2/CNT nano-composite interlayers on mechanically strong ceramic substrates was able to finely tailor desirable properties such as surface pore size and surface roughness to provide a versatile platform for polyamide formation via IP reaction.

Properties of Ceramic-based TFC-FO Membranes

After the formation of the PA layer, the M-PA, M-T-PA and M-T/CNT-PA membranes exhibited different surface and structure morphologies (Figure 3). For the coarse mullite substrate without interlayer, the PA layer had greater thickness and larger pores (possibly defects) in its surface, and the commonly reported ridge-and-valley structure could not be observed clearly (Figure 3a,d). Furthermore, the cross section of this membrane did not show the typical presence of nanovoids reported for MPD-TMC based polyamide layers.[34-38] According to Tang and co-workers,[27,34,38-40] the formation of ridge-and-valley structure and the nanovoids inside the polyamide layer was driven by the degassing of nanosized CO_2 bubbles as a result of the reduced CO_2 solubility in the aqueous MPD solution since HCl and heat

were released during the IP reaction. The subsequent encapsulation of these CO_2 nanobubbles between the substrate and the polyamide film results in the nanovoids-containing surface protuberances that are known as the ridge-and-valley features.[27] In the current study, the mullite substrate with very large surface pores (mean pore size ~ 475 ± 24 nm, Figure S6a) may not be able to effectively retain the nanobubbles[27] and therefore could not effectively develop the ridge-and-valley structure.

After coating with TiO_2 or TiO_2/CNT interlayers, the resulting M-T-PA and M-T/CNT-PA membranes featured nanovoid-containing ridge-and-valley features for their PA layers (Figure 3b,e and Figure 3c,f, respectively), which can be explained by the smaller surface pores and lower surface roughness of their substrates. Compared to M-T-PA, M-T/CNT-PA had greater presence of nanovoids inside its PA layer (Figure 3e,f) together with slightly higher surface roughness (55 ± 2 nm vs. 61 ± 3 nm, see Figure 3h,i) despite the use of a much smoother substrate (Figure 2l), thanks to the greater confinement effect[27] on the degassed nanobubbles due to the reduced surface pore size. According to literature,[27,34,37-40] the effective creation of nanovoids would be beneficial for enhancing membrane permeability by significantly increasing the effective filtration area of the PA film. In the current study, the M-T-PA and M-T/CNT-PA membrane possessed a clear interface between PA layer and TiO_2 or CNT interlayer, respectively, while there is no obvious boundary between PA layer and mullite substrate (Figures 3d-f). This was possibly due to the penetration and growth of the PA layer inside the pores of coarse mullite substrate. Our results are

consistent with a prior study reporting the effectiveness of interlayer for preventing the intrusion of polyamide into the substrate.[41]

The XPS results show only the presence of O, N, and C elements on the three PA membrane surfaces, confirming the formation of polyamide layer. The M-T/CNT-PA membrane exhibited the lowest O/N ratio among the three membranes, suggesting a higher cross-linking degree compared to M-PA and M-T-PA membranes (Figures 3j-l). This beneficial effect can be explained by the greater sorption of MPD with the presence of additional interlayers.[41]

Table 1. Transport and structural properties of ceramic-based TFC-FO membranes.

Membranes	Water permeability [a] (A, L/(m^2 h bar)	Salt permeability (B, L/(m^2 h)	B/A (bar^{-1})	Salt rejection [b] R_s (%)	Structural parameter [c] (S, μm)
M-PA	1.3 ± 0.3	0.92 ± 0.12	0.70	92.2 ± 3.6	568 ± 45
M-T-PA	1.2 ± 0.1	0.77 ± 0.08	0.64	96.0 ± 1.9	317 ± 23
M-T/CNT-PA	2.0 ± 0.1	0.58 ± 0.03	0.29	98.0 ± 1.7	248 ± 20

[a] Evaluated in a RO setup at 5 bar trans-membrane pressure against deionized water.

[b] Evaluated in a RO setup at 5 bar trans-membrane pressure with 200 ppm NaCl as feed.

[c] Calculated under PRO mode using 1 M NaCl as draw solution and DI water as feed.

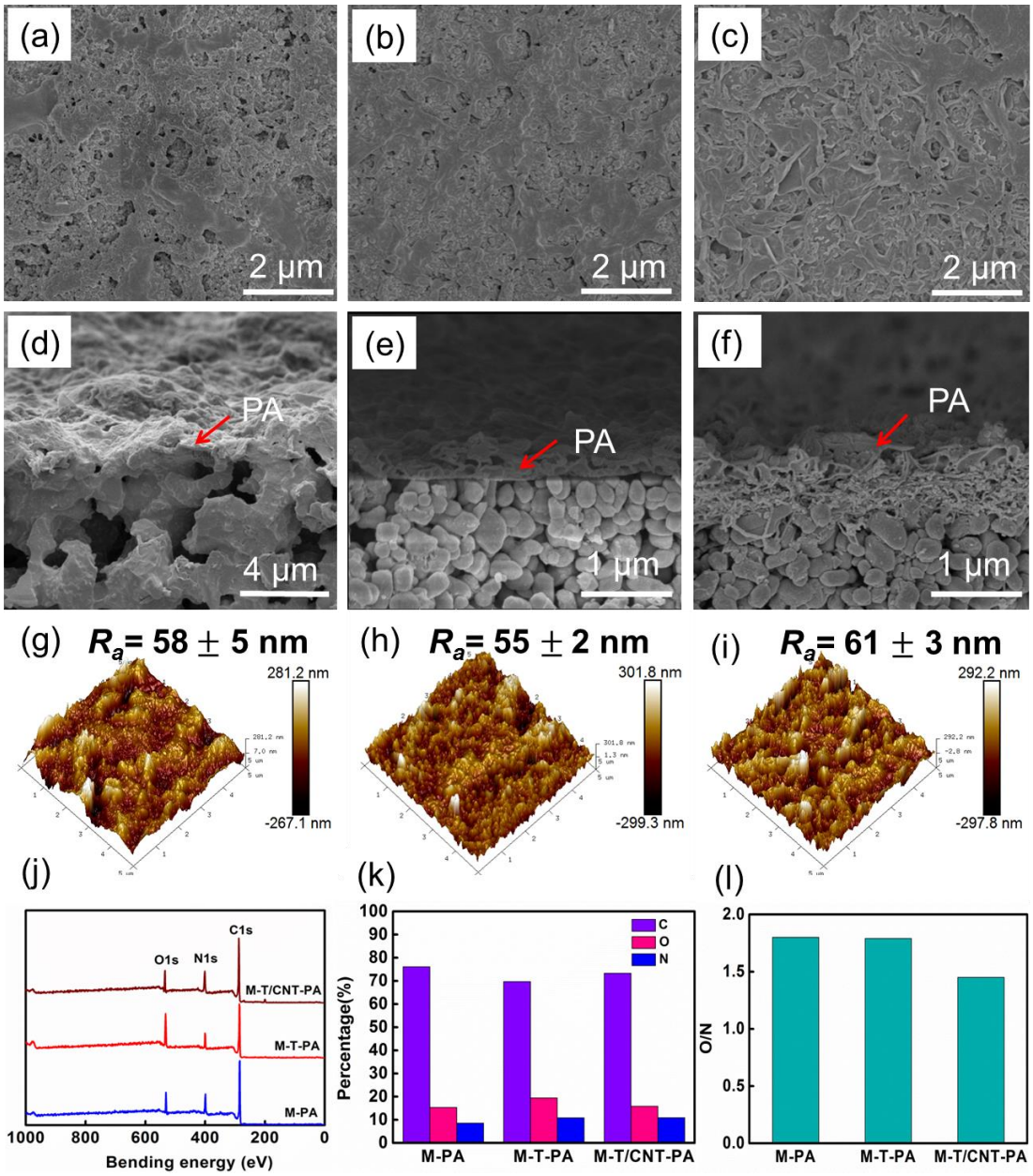

Figure 3. Surface SEM images of (a) M-PA membrane (b) M-T-PA membrane and (c) M-T/CNT-PA membrane; cross sections SEM images of (d) M-PA membrane and (e) M-T-PA membrane (f) M-T/CNT-PA membrane; AFM images of (g) M-PA, (h) M-T-PA and (i) M-T/CNT-PA membrane; (j) surface XPS spectra, (k) elemental composition and (l) O/N ratio of M-PA, M-T-PA and M-T/CNT-PA membranes.

Compared with M-PA and M-T-PA membrane, M-T/CNT-PA membrane exhibited higher water permeability (A), higher salt rejection and lower salt permeability (Table

1). The ratio of solute permeability to water permeability (*B/A*) is a direct indicator of membrane selectivity. The M-T/CNT-PA membrane has a lower *B/A* ratio of only ~0.29 bar^{-1}, indicating a higher selectivity of water over salt due to the existence of less defects (Figure 3c) and higher cross-linking degree of the PA layer (Figure 3l). Structure parameter (*S*) value is an important parameter for FO performance to reflect ICP inside FO membrane, which depends strongly on the properties of membrane substrate. The *S* value of M-T/CNT-PA membrane was only 248 ± 20 μm, which is lower than those of M-T-PA and M-PA membrane (317 ± 23 and 568 ± 45 μm, respectively). This value is also considerably lower than that of commercial CTA FO membranes (950 μm) and most of the state-of-the-art TFC-FO membranes (Table S4). Although freestanding GO-based FO membranes possess lower *S* values,[42] these membranes without support suffered from low mechanical stability and are difficult to scale up. Our results may suggest that the polyamide formed in the pores reduced effective porosity that hindered solute diffusion while the presence of TiO_2 and TiO_2/CNT interlayer accelerated the solute diffusion.[29]

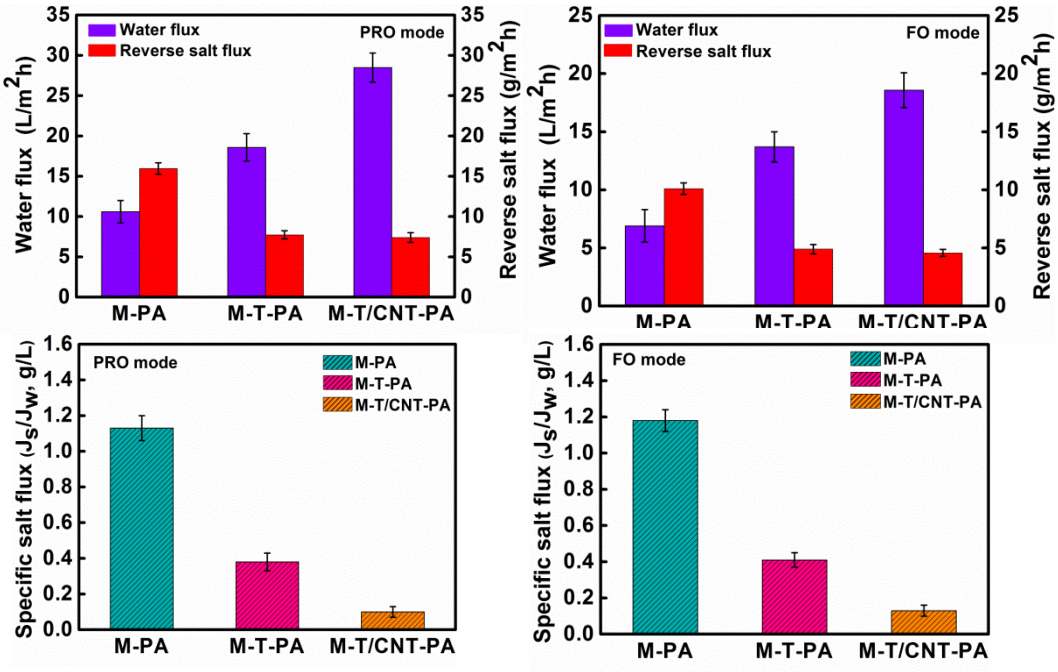

Figure 4. FO performance (water flux and reverse salt flux) of M-PA, M-T-PA and M-T/CNT-PA membranes: (a) under PRO mode, (b) under FO mode; specific salt flux (J_s/J_w) of M-PA, M-T-PA and M-T/CNT-PA membranes: (c) under PRO mode, (d) under FO mode. Feed: DI water. Draw solution: 1 M NaCl.

In PRO mode, compared with that of M-PA membrane (10.6 ± 1.4 L/m^2 h), coating of TiO_2 layer improved the water flux (18.6 ± 1.7 L/m^2 h) of M-T-PA membrane by ~ 75% since this interlayer prevented the formation of polyamide inside macro-porous mullite substrate and thus reduced the effective thickness of PA top-layer with decreased water transfer resistance.[25,41] In comparison, coating of TiO_2/CNT interlayers resulted in a more significantly enhanced water flux (28.5 ± 1.8 L/m^2 h) (Figures 4a-b), 168% higher than that of the membrane without any interlayer. This special CNT-constructed network layer was beneficial to the formation of PA layer

with a rougher surface and greater presence of nanovoids, which provided larger effective membrane surface area and more free space for rapid high-flux water transport.[27,37-40,43,44] In addition, the reduced S value of M-T/CNT-PA also helps to maintain a higher water flux. Similar trend was observed for the FO mode. Furthermore, the M-T/CNT-PA shows the lowest specific reverse solute flux (J_s/J_v) for both PRO and FO mode (Figure 4c,d), which is consistent with its highest rejection and lowest B/A values (Table 1). Compared to the commercial CTA membrane and most of the state-of-the-art TFC-FO polymeric membranes, the ceramic-based M-T/CNT-PA membrane developed in this work showed higher water flux and comparable reverse salt flux (Table S4).

For M-PA, M-T-PA and M-T/CNT-PA membranes, the water flux exhibited similarly increasing trends with increasing NaCl concentration in both FO and PRO modes (Figures 5a-b) due to the greater osmotic driving force. Similarly, the reverse salt flux also increased when the concentration of NaCl draw solution increased (Figures 5c-d). Nevertheless, the J_s/J_v ratio remained relatively constant for any given membrane regardless of the membrane orientation (Figures 5e-f) since this ratio is determined by the inherent selectivity parameter (B/A) of the membranes.[45] Among the three membranes, the M-T/CNT-PA membrane had the combination of lowest J_s/J_w ratio and highest water flux under any given testing conditions.

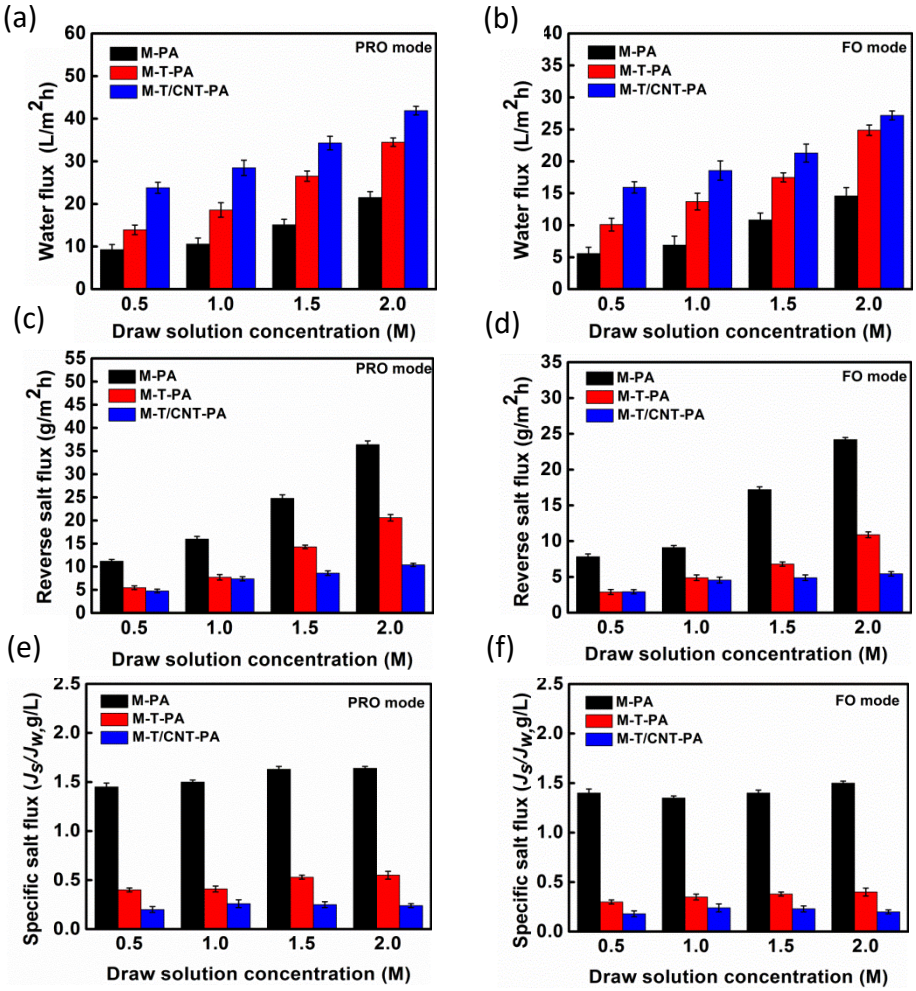

357

358 **Figure 5.** Water flux, reverse salt flux and specific salt flux of M-PA, M-T-PA and

359 M-T/CNT-PA membranes with DI water as feed solution against different draw solution

360 concentrations (0.5−2 M): under PRO mode (a, c, e) and under FO mode(b, d, f).

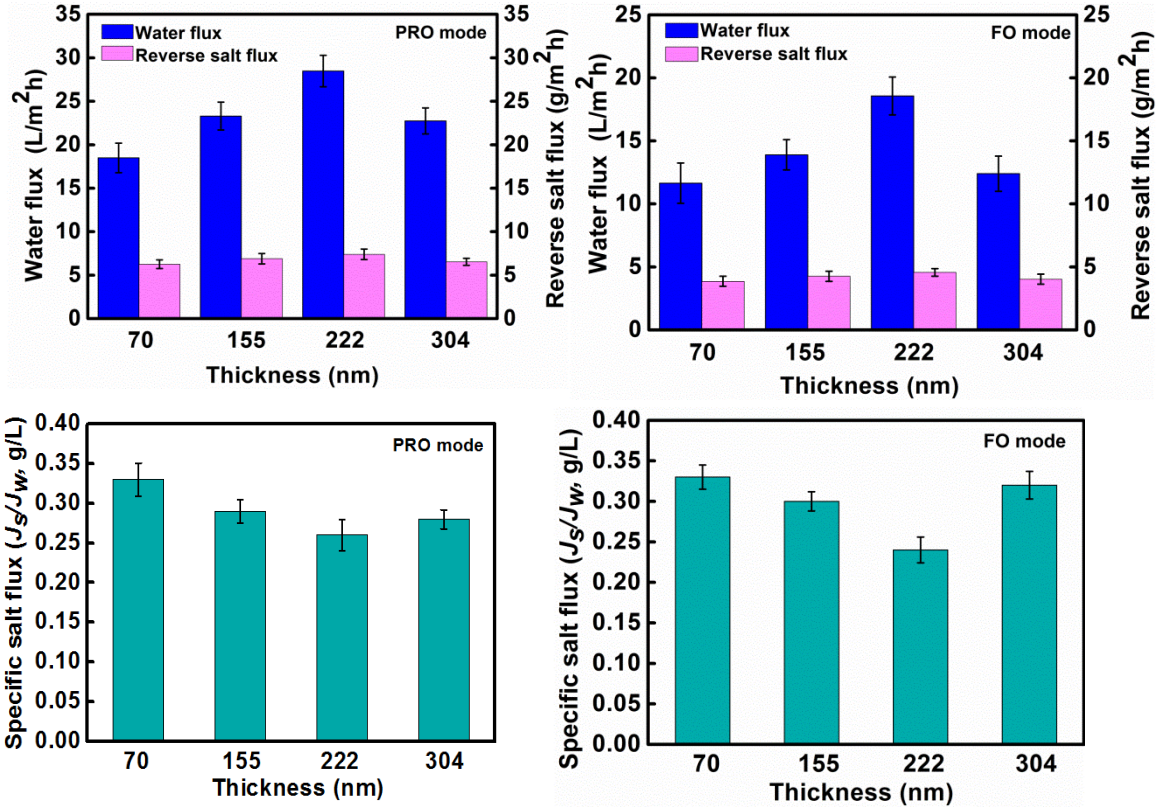

Figure 6. FO performance (water flux, reverse salt flux and specific salt flux) of M-T/CNT-PA membranes with different thickness of CNT interlayer: (a) under PRO mode and (b) under FO mode. Feed: DI water. Draw solution: 1 M NaCl.

The thickness of CNT interlayer was crucial to affect the FO performance of the final M-T/CNT-PA membranes in both PRO and FO modes (Figure 6). Thick CNT interlayer provided more free space for water transport and also larger effective membrane area of the final PA layer, consequently enhancing water flux.[46] A gradual increase in water flux was observed with initial increasing CNT thickness, where a maximum water flux (28.5 ± 1.8 L/m^2 h) was obtained at 222 nm thickness. Nevertheless, further increasing the CNT layer thickness to 304 nm decreased the water flux to 22.7 ± 1.5 L/m^2 h, which could be due to the dominance of the hydraulic

resistance of the thicker CNT layer. In comparison, reverse salt flux was largely independent of the CNT interlayer thickness due to the formation of defect-free PA top-layers featuring their excellent cross-linking degrees.[46,47]

Mechanism Insight into Membrane Formation and Water/Salt Transport

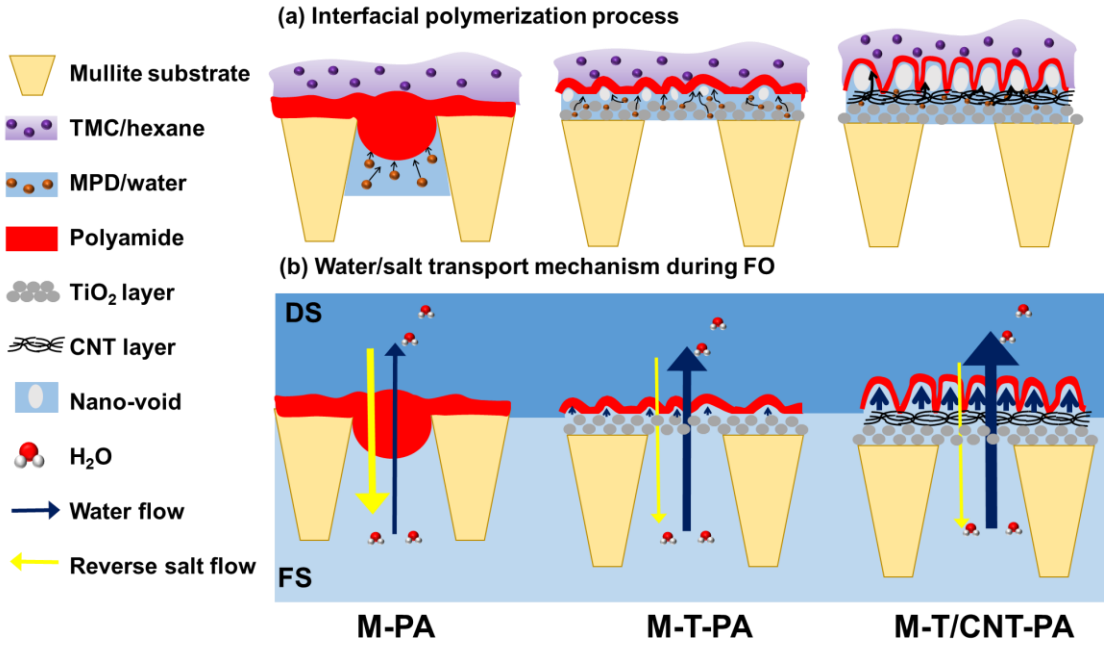

Figure 7. (a) Conceptual illustration of formation mechanism of PA selective layer on different ceramic-based substrates and (b) water and reverse salt transport mechanism across ceramic-based TFC-FO membranes with different interlayers.

A mechanism insight is proposed here to understand the role of nano-composite interlayer for membrane formation during IP and membrane transport during FO process (Figure 7). As illustrated in Figure 7a, when interfacial polymerization occurred on a coarse mullite substrate without any interlayer, polyamide grew deeper inside the macro-pores of the rough mullite substrate due to the insufficient retention by its large surface pores.[41] This led to the formation of a thicker PA layer with more

387 defects and lower cross-linking degree.[24] Such a thick PA layer, which was
388 penetration-grown inside coarse mullite substrate, had higher effective membrane
389 thickness, significantly enhancing water permeation resistance and consequently
390 exhibiting lower water permeability during FO process (Figures 4a-b).[41] In addition,
391 the defects formed in this PA layer allowed salt permeation with lower transport
392 resistance, showing higher salt permeability. By comparison, however, coating of
393 TiO_2 interlayer and especially TiO_2/CNT nano-composite interlayer exhibited
394 significantly improved surface characteristics. The resulting smaller pore size and
395 smoother surface not only hinder the penetration of polyamide into the substrates,
396 but also result in the formation of much thinner PA layers.[15,41] Such thinner PA layers
397 also features less defects, greater effective filtration area (due to the greater presence
398 of nanovoid-containing roughness features) and better cross-linking degree.
399 Importantly, CNT interlayer acted as a highly porous three dimension network
400 structure for not only allowing rapid high-flux water transport but also providing
401 more active sites for the growth of PA roughness features.[29,46] Furthermore, this
402 structure features a reduced structural parameter. The corresponding M-T/CNT-PA
403 membrane therefore achieved the greatest improvements in water permeability, salt
404 rejection while lower reverse salt flux.

405 **IMPLICATIONS**

406 In this study, with introduction of TiO_2/CNT nano-composite interlayer, a rational
407 structure design strategy was proposed to fabricate high-performance mullite

ceramic-based FO membrane featuring enhanced water flux and salt rejection with lowered reverse salt flux. The mullite substrate exhibited excellent hydrophilcity and water wettability, high porosity (74%-finger-like macro-voids) and high water flux. Coating of TiO_2/CNT interlayers on coarse mullite substrates slightly altered surface porosity, mechanical and hydrophilic properties, but effectively decrease pore size and surface roughness, endowing better membrane surface characteristic for interface polymerization. This could not only significantly hinder the penetration growth of polyamide into the substrates, but result in the formation of much thinner PA layers featuring less defects, higher surface roughness with more nano-voids, larger effective filtration area and better cross-linking degree. As a result, the final ceramic-based TFC-FO membrane with TiO_2/CNT nano-composite interlayer possessed higher water flux, salt rejection and lower reverse salt flux than TFC-FO membrane without any interlayer. In addition, the introduction of TiO_2/CNT interlayers is an effective strategy to reduce the ICP of FO membrane with lower *S* value. These suggest that a high-performance ceramic-based FO membrane can be produced by applying TiO_2/CNT nano-composite interlayer on ceramic substrate, showing a great potential in FO process. Although the current study employed vacuum filtration for the loading of CNTs, future studies may further explore other alternatives such as spray-coating and dip-coating.[21,29,48]

Compared to commercially available polymeric FO membranes, ceramic membranes are known to have better mechanical strength and chemical stability. Even though FO requires no applied pressure, pilot studies show that hydraulic pressures of

a few bar can occur at the inlet to membrane modules,[49] which causes membrane deformation and deterioration of separation properties.[50] Prior studies have also reported damage of FO membranes due to scaling formation, which is largely due to the weak mechanical properties of commercially available polymeric FO membranes.[51,52] The ceramic-based FO membrane with high mechanical strength is beneficial to address these issues. Furthermore, the development of mechanically strong osmotically-driven membranes will further enable additional applications such as pressure retarded osmosis and pressure assisted osmosis, for which mechanical stability is one of the critical concerns.[53-57] In addition to improved mechanical strength, the ceramic-based FO membranes also offer better chemical stability compared to traditional polymeric FO membranes, which allows their use for some harsh applications, e.g., organic solvent filtration.[57,58] Studies show that polyamide nanofiltration membranes prepared on ceramic substrates have better resistance to various organic solvents.[59,60] Future studies are needed to explore the use of ceramic-based FO membranes for organic solvent filtration.

ASSOCIATED CONTENT

Supporting Information

S1. Fabrication and characterization of ceramic-based TFC-FO membranes (Figures S1-S3, Tables S1 and S2); S2. Optimization of hollow fiber ceramic substrate (Figures S4 and S5); S3. Cost analysis (Table S3); S4. Formation mechanism of mullite substrate structure; S5. Surface properties of M, M-T and M-T/CNT

membrane substrates (Figure S6); S6. Optimization of synthesis conditions for PA layer (Figures S7 and S8); S7. Stability of membranes (Figure S9); S8. Comparison of FO performances (Table S4).

AUTHOR INFORMATION

Corresponding authors:

Chuyang Y. Tang (tangc@hku.hk)

Yingchao Dong (ycdong@dlut.edu.cn)

ORCID

1, Chuyang Y. Tang: 0000-0002-7932-6462

2, Yingchao Dong: 0000-0003-1409-0994

Notes

The authors declare no competing financial interest.

ACKNOWLEDGEMENTS

This work was financially supported by the National Natural Science Foundation of China (No. 21876020), Youth Top-Notch Talent Program of Talent Project of Revitalizing Liaoning (No. XLYC1807250), National Key Research and Development Project (No. 2019YFA0705803), Key Project of Liaoning Natural Science Foundation (No. 20180510005), the Haitian Scholar Program from Dalian University of Technology, and the 111 Program of Introducing Talents of Discipline to Universities (No. B13012). We also thank Mr. Chunyi Sun for helpful discussions on

471 this work.

472 **REFERENCES**

473 (1) Shannon, M. A., Bohn, P. W., Elimelech, M., Georgiadis, J. G., Marinas, B. J., Mayes, A. M.
474 Science and technology for water purification in the coming decades. *Nature* **2010**, *452*, 301-310.
475 (2) Greenlee, L. F., Lawler, D. F., Freeman, B. D., Marrot, B., & Moulin, P. Reverse osmosis
476 desalination: water sources, technology, and today's challenges. *Water Res*. **2009**, *43* (9),
477 2317-2348.
478 (3) Dong, Y., Ma, L., Tang, C.Y., Yang, F., Quan, X., Jassby, D., Zaworotko, M.J., Guiver, M.D.
479 Stable superhydrophobic ceramic-based carbon nanotube composite desalination membranes.
480 *Nano Lett*. **2018**, *18* (9), 5514-5521.
481 (4) Cath, T. Y., Childress, A. E., Elimelech, M. Forward osmosis: principles, applications, and
482 recent developments. *J. Membr. Sci*. **2006**, *281* (1-2), 70-87.
483 (5) She, Q., Wang, R., Fane, A. G., Tang, C. Y. Membrane fouling in osmotically driven
484 membrane processes: A review. *J. Membr. Sci*., **2016**, *499*, 201-233.
485 (6) Ly, Q. V., Hu, Y., Li, J., Cho, J., Hur, J. Characteristics and influencing factors of organic
486 fouling in forward osmosis operation for wastewater applications: A comprehensive review.
487 *Environ. Int.* **2019**, *129*, 164-184.
488 (7) Martinetti, C. R., Childress, A. E., Cath, T. Y. High recovery of concentrated RO brines using
489 forward osmosis and membrane distillation. *J. Membr. Sci*. **2009**, *331* (1-2), 31-39.
490 (8) Wang, X., Chang, V. W., Tang, C. Y. Osmotic membrane bioreactor (OMBR) technology for
491 wastewater treatment and reclamation: Advances, challenges, and prospects for the future. *J.*
492 *Membr. Sci*. **2016**, *504*, 113-132.
493 (9) Wang, R., Shi, L., Tang, C. Y., Chou, S., Qiu, C., Fane, A. G. Characterization of novel
494 forward osmosis hollow fiber membranes. *J. Membr. Sci*. **2010**, *355* (1-2), 158-167.
495 (10) Yip, N. Y., Tiraferri, A., Phillip, W. A., Schiffman, J. D., Elimelech, M. High performance
496 thin-film composite forward osmosis membrane. *Environ. Sci. Technol*. **2010**, *44* (10), 3812-3818.
497 (11) Fang, W., Wang, R., Chou, S., Setiawan, L., Fane, A. G. Composite forward osmosis hollow
498 fiber membranes: Integration of RO-and NF-like selective layers to enhance membrane properties
499 of anti-scaling and anti-internal concentration polarization. *J. Membr. Sci*. **2012**, *394*, 140-150.
500 (12) Ma, N., Wei, J., Qi, S., Zhao, Y., Gao, Y., Tang, C. Y. Nanocomposite substrates for
501 controlling internal concentration polarization in forward osmosis membranes. *J. Membr. Sci*.
502 **2013**, *441*, 54-62.
503 (13) Shi, S. J., Pan, Y. H., Wang, S. F., Dai, Z. W., Gu, L., Wu, Q. Y. Aluminosilicate Nanotubes
504 Embedded Polyamide Thin Film Nanocomposite Forward Osmosis Membranes with
505 Simultaneous Enhancement of Water Permeability and Selectivity. *Polymers*, **2019**, *11* (5), 879.
506 (14) Zhang, S., Wang, K. Y., Chung, T. S., Chen, H., Jean, Y. C., Amy, G. Well-constructed
507 cellulose acetate membranes for forward osmosis: minimized internal concentration polarization
508 with an ultra-thin selective layer. *J. Membr. Sci*. **2010**, *360* (1-2), 522-535.
509 (15) Zhao, W., Liu, H., Liu, Y., Jian, M., Gao, L., Wang, H., Zhang, X. Thin-film nanocomposite
510 forward-osmosis membranes on hydrophilic microfiltration support with an intermediate layer of

graphene oxide and multiwall carbon nanotube. *ACS Appl. Mater. Interfaces* **2018**, *10* (40), 34464-34474.
(16) Widjojo, N., Chung, T. S., Weber, M., Maletzko, C., Warzelhan, V. The role of sulphonated polymer and macrovoid-free structure in the support layer for thin-film composite (TFC) forward osmosis (FO) membranes. *J. Membr. Sci*. **2011**, *383* (1-2), 214-223.
(17) Chou, S., Wang, R., Fane, A. G. Robust and high performance hollow fiber membranes for energy harvesting from salinity gradients by pressure retarded osmosis. *J. Membr. Sci*. **2013**, *448*, 44-54.
(18) Zhao, S., Zou, L., Tang, C. Y., Mulcahy, D. Recent developments in forward osmosis: opportunities and challenges. *J. Membr. Sci*. **2012**, *396*, 1-21.
(19) You, S., Tang, C., Yu, C., Wang, X., Zhang, J., Han, J., Ren, N. Forward osmosis with a novel thin-film inorganic membrane. *Environ. Sci. Technol*. **2013**, *47* (15), 8733-8742.
(20) Lu, D., Zhang, T., Ma, J. Ceramic membrane fouling during ultrafiltration of oil/water emulsions: roles played by stabilization surfactants of oil droplets. *Environ. Sci. Technol*. **2015**, *49* (7), 4235-4244.
(21) Zhu, L., Chen, M., Dong, Y., Tang, C. Y., Huang, A., Li, L. A low-cost mullite-titania composite ceramic hollow fiber microfiltration membrane for highly efficient separation of oil-in-water emulsion. *Water Res*. **2016**, *90*, 277-285.
(22) Fan, X., Liu, Y., Quan, X., Chen, S. Highly permeable thin-film composite forward osmosis membrane based on carbon nanotube hollow fiber scaffold with electrically enhanced fouling resistance. *Environ. Sci. Technol*. **2018**, *52* (3), 1444-1452.
(23) Chen, M., Zhu, L., Dong, Y., Li, L., Liu, J. Waste-to-resource strategy to fabricate highly porous whisker-structured mullite ceramic membrane for simulated oil-in-water emulsion wastewater treatment. *ACS Sustain. Chem. Eng*. **2016**, *4* (4), 2098-2106.
(24) Ghosh, A. K., Hoek, E. M. Impacts of support membrane structure and chemistry on polyamide–polysulfone interfacial composite membranes. *J. Membr. Sci*. **2009**, *336* (1-2), 140-148.
(25) Fathizadeh, M., Aroujalian, A., Raisi, A. Effect of lag time in interfacial polymerization on polyamide composite membrane with different hydrophilic sub layers. *Desalination* **2012**, *284*, 32-41.
(26) Jimenez-Solomon, M. F., Gorgojo, P., Munoz-Ibanez, M., Livingston, A. G. Beneath the surface: Influence of supports on thin film composite membranes by interfacial polymerization for organic solvent nanofiltration. *J. Membr. Sci*. **2013**, *448*, 102-113.
(27) Song, X., Gan, B., Yang, Z., Tang, C. Y., Gao, C. Confined nanobubbles shape the surface roughness structures of thin film composite polyamide desalination membranes. *J. Membr. Sci*. **2019**, *582*, 342-349.
(28) Yang, Z., Guo, H., Tang, C. Y. The upper bound of thin-film composite (TFC) polyamide membranes for desalination. *J. Membr. Sci*. **2019**, *590*, 117297.
(29) Zhou, Z., Hu, Y., Boo, C., Liu, Z., Li, J., Deng, L., An, X. High-performance thin-film composite membrane with an ultrathin spray-coated carbon nanotube interlayer. *Environ. Sci. Technol. Lett*. **2018**, *5* (5), 243-248.
(30) Lee, H., Dellatore, S. M., Miller, W. M., Messersmith, P. B. Mussel-inspired surface chemistry for multifunctional coatings. *Science* **2007**, *318*, 426–430.
(31) Xu, K., Feng, B., Zhou, C., Huang, A. Synthesis of highly stable graphene oxide membranes

555 on polydopamine functionalized supports for seawater desalination. *Chem. Eng. Sci.* **2016**, *146*,
556 159-165.
557 (32) Chen, M., Zhu, L., Chen, J., Yang, F., Tang, C. Y., Guiver, M. D., Dong, Y. Spinel-based
558 ceramic membranes coupling solid sludge recycling with oily wastewater treatment. *Water Res*.
559 **2020**, *169*, 115180.
560 (33) Kingsbury, B. F. K., Li, K. A morphological study of ceramic hollow fibre membranes. *J.*
561 *Memb. Sci*. **2009**,*328*, 134-140.
562 (34) Song, X., Gan, B., Qi, S., Guo, H., Tang, C. Y., Zhou, Y., Gao, C. Intrinsic Nanoscale
563 structure of thin film composite polyamide membranes: connectivity, defects, and structure–
564 property correlation. *Environ. Sci. Technol*. **2020**, *54* (6), 3559-3569.
565 (35) Kłosowski, M. M., McGilvery, C. M., Li, Y., Abellan, P., Ramasse, Q., Cabral, J. T., Porter, A.
566 E. Micro-to nano-scale characterisation of polyamide structures of the SW30HR RO membrane
567 using advanced electron microscopy and stain tracers. *J. Membr. Sci*. **2016**, *520*, 465-476.
568 (36) Culp, T. E., Shen, Y. X., Geitner, M., Paul, M., Roy, A., Behr, M. J., Gomez, E. D. Electron
569 tomography reveals details of the internal microstructure of desalination membranes. *Proceedings*
570 *of the National Academy of Sciences* **2018**, *115* (35), 8694-8699.
571 (37) Song, X., Smith, J. W., Kim, J., Zaluzec, N. J., Chen, W., An, H., Chen, Q. Unraveling the
572 Morphology–Function Relationships of Polyamide Membranes Using Quantitative Electron
573 Tomography. *ACS Appl. Mater. Interfaces* **2019**, *11* (8), 8517-8526.
574 (38) Ma, X. H., Yao, Z. K., Yang, Z., Guo, H., Xu, Z. L., Tang, C. Y., Elimelech, M. Nanofoaming
575 of polyamide desalination membranes to tune permeability and selectivity. *Environ. Sci. Technol.*
576 *Lett*. **2018**, *5* (2), 123-130.
577 (39) Ma, X., Yang, Z., Yao, Z., Guo, H., Xu, Z., Tang, C. Y. Tuning roughness features of thin film
578 composite polyamide membranes for simultaneously enhanced permeability, selectivity and
579 anti-fouling performance. *J. Colloid Interface Sci*. **2019**, *540*, 382-388.
580 (40) Peng, L. E., Yao, Z., Liu, X., Deng, B., Guo, H., Tang, C. Y. Tailoring Polyamide Rejection
581 Layer with Aqueous Carbonate Chemistry for Enhanced Membrane Separation: Mechanistic
582 Insights, Chemistry-Structure-Property Relationship, and Environmental Implications. *Environ.*
583 *Sci. Technol*. **2019**, *53* (16), 9764-9770.
584 (41) Yang, Z., Zhou, Z. W., Guo, H., Yao, Z., Ma, X. H., Song, X., Tang, C.Y. Tannic acid/Fe^{3+}
585 nanoscaffold for interfacial polymerization: toward enhanced nanofiltration performance. *Environ.*
586 *Sci. Technol*. **2018**, *52* (16), 9341-9349.
587 (42) Zhao, Y., Wang, X., Ren, Y., Pei, D. Mesh-embedded Polysulfone/Sulfonated Polysulfone
588 supported thin film composite membranes for forward osmosis. *ACS Appl. Mater. Interfaces* **2018**,
589 *10* (3), 2918-2928.
590 (43) Huang, L., McCutcheon, J. R. Impact of support layer pore size on performance of thin film
591 composite membranes for forward osmosis. *J. Membr. Sci*. **2015**, *483*, 25-33.
592 (44) Phillip, W. A., Yong, J. S., Elimelech, M. Reverse draw solute permeation in forward osmosis:
593 modeling and experiments. *Environ. Sci. Technol*. **2010**, *44* (13), 5170-5176.
594 (45) Tang, C. Y., She, Q., Lay, W. C., Wang, R., Fane, A. G. Coupled effects of internal
595 concentration polarization and fouling on flux behavior of forward osmosis membranes during
596 humic acid filtration. *J. Membr. Sci*. **2010**, *354* (1-2), 123-133.
597 (46) Zhao, X., Li, J., Liu, C. A novel TFC-type FO membrane with inserted sublayer of carbon
598 nanotube networks exhibiting the improved separation performance. *Desalination* **2017**, *413*,

599 176-183.
600 (47) Gong, G., Wang, P., Zhou, Z., Hu, Y. New insights into the role of an interlayer for the
601 fabrication of highly selective and permeable thin-film composite nanofiltration membrane. *ACS*
602 *Appl. Mater. Interfaces* **2019**, *11* (7), 7349-7356.
603 (48) Dong, Y., Chen, S., Zhang, X., Yang, J., Liu, X., Meng, G. Fabrication and characterization of
604 low cost tubular mineral-based ceramic membranes for micro-filtration from natural zeolite. *J.*
605 *Membr. Sci*. **2006**, *281*, 592-599.
606 (49) Kim, J. E., Phuntsho, S., Ali, S. M., Choi, J. Y., Shon, H. K. Forward osmosis membrane
607 modular configurations for osmotic dilution of seawater by forward osmosis and reverse osmosis
608 hybrid system. *Water Res.* **2018**, *128*, 183-192.
609 (50) Lee, C., Jang, J., Tin, N. T., Kim, S., Tang, C. Y., Kim, I. S. Effect of spacer configuration on
610 the characteristics of FO membranes: Alteration of permeation characteristics by membrane
611 deformation and concentration polarization. *Environ. Sci. Technol*. **2020**. DOI:
612 10.1021/acs.est.9b06921
613 (51) Wang, Y., Eliisa, J., Wei, J., Zhang, M., Hanna, K., Wang, R., Tang, C. Y. Gypsum scaling and
614 membrane integrity of osmotically driven membranes: The effect of membrane materials and
615 operating conditions. *Desalination* **2016**, *377*, 1-10.
616 (52) Xie, M., Tang, C. Y., Gray, S. R. Spacer-induced forward osmosis membrane integrity loss
617 during gypsum scaling. *Desalination* **2016**, *392*, 85-90.
618 (53) She, Q., Hou, D., Liu, J., Tan, K. H., Tang, C. Y. Effect of feed spacer induced membrane
619 deformation on the performance of pressure retarded osmosis (PRO): Implications for PRO
620 process operation. *J. Membr. Sci*. **2013**, *445*, 170-182.
621 (54) Kim, Y. C., Kim, Y., Oh, D., Lee, K. H. Experimental Investigation of a Spiral-Wound
622 Pressure-Retarded Osmosis Membrane Module for Osmotic Power Generation. *Environ. Sci.*
623 *Technol*. **2013**, *47* (6), 2966-2973.
624 (55) Blandin, G., Verliefde, A. R. D., Tang, C. Y., Childress, A. E., Le-Clech, P. Validation of
625 assisted forward osmosis (AFO) process: Impact of hydraulic pressure. *J. Membr. Sci*. **2013**, *447*,
626 1-11.
627 (56) Lee, E. S. H., Xiong, J. Y., Han, G., Wan, C. F., Chong, Q. Y., Chung, T. S. A pilot study on
628 pressure retarded osmosis operation and effective cleaning strategies. *Desalination* **2017**, *420*,
629 273-282.
630 (57) Cui, Y., Chung, T. S. Solvent recovery via organic solvent pressure assisted osmosis. *Ind. Eng.*
631 *Chem. Res.* **2019**, *58* (12), 4970-4978.
632 (58) Li, B., Japip, S., Chung, T. S. Molecularly tunable thin-film nanocomposite membranes with
633 enhanced molecular sieving for organic solvent forward osmosis. *Nat. Commun.* **2020**, *11* (1),
634 1198.
635 (59) Xia, L. McCutcheon, J. R. Understanding the influence of solvents on the intrinsic properties
636 and performance of polyamide thin film composite membranes. *Sep. Purif. Technol.* **2020**, *238*,
637 116398.
638 (60) Xia, L., Jian, R., Marcus, W., Mccutcheon, J. R. Ceramic-supported thin film composite
639 membrane for organic solvent nanofiltration. *J. Membr. Sci.* **2018**, *563*, 857-863.
640
641
642